DIFFERENCES IN FORCED AND DECAYING MODES IN LABORATORY ZONAL JET SIMULATIONS

EVAN DAVID WELLMEYER

M.Sc. Atmospheric Science and Technology

Course in Advanced Fluid Mechanics

Dr. Stefania Espa

Università Degli Studi Dell'Aquila, L'Aquila

Sapienza Università Di Roma, Rome

Spring 2021

1 Introduction

Zonation in atmospheric flows are a topic of particular interest as it has relevance not only to the Earth's atmosphere but also in gas giants such as Jupiter and Saturn. In Earth's atmosphere there is a dominance of westerly zonal jets, whereas stratified zonal flows in both directions are present in the gas giants [1]. Westerly jets on Earth can be held accountable for a significant portion of surface weather events [2]. The large scale motion of these flows has been considered by many as quasi-two-dimensional to a first approximation [3][4]. The jets owe their existence to the restoring force associated with the latitudinal variation of the Coriolis parameter, $f = 2\Omega \sin\theta$, where Ω is the angular velocity of the planetary rotation, and θ is the latitude [5], this is the well known f-plane approximation. The variation in the f-plane is known as the β-plane and is measured as $\beta = (1/R)df/d\theta = 2(\Omega/R)\cos\theta$, where R is the planetary radius [5]. The impact of this latitudinal variation is known as the β-effect. The β-effect-related force is comparable to an elastic force as it tends to return a displaced fluid particle to its equilibrium latitude, giving rise to fluctuations around that latitude known as the Rossby waves [5]. A fluid with a β effect is said to exhibit Rossby wave elasticity [6].

Likely mechanisms of formation and maintenance of the zonal jets have been identified in a variety of experiments. The first of which is redirection of the inverse energy cascade into zonal modes due to turbulence-waves interaction [7][8][9]. The union of turbulence and waves characteristic of of large-scale planetary circulations can be thought of as macroturbulence [10]. Other potential mechanisms include the horizontal mixing of potential vorticity [5][11], planetary rotation and stable stratification facilitate material conservation of potential vorticity [5]. Baroclinic instability and baroclinic eddy-mean flow interactions [12][13][14] and β-plume perturbation [4][15] have also emerged as potential mechanisms of zonation. However, one of the most important theories attributes the process of zonation to anisotropic inverse energy cascade [16] [4].

Many methods have been used to reproduce these zonal jets in the laboratory with rotating tanks in order to develop such theories. Common methods include air bubbles rising from a vertically oscillating pipe, differential heating where the inner walls are cooled or the outer walls are heated, or even the continuous spraying of dense salty water onto the fluid surface. A particularly effective way of reproducing zonal flows is using electromagnetic forcing in a rotating tank of salinated water. In this experiment, EM forcing was used to observe the emergence and evolution of zonal jet-like structures and the subsequent decay of matured flows in the absence of forcing. As the tank spins, the variation of the fluid height with radius produces a topographic γ effect causing flow anisotropization and zonation, barotropic instability across the jet breaks the jet up into waves [5].

2 Theory

The simulation of zonation via electromagnetic forcing is done by rotating a tank filled with an electrolytic solution. In the presence of background rotation, the free-surface of the fluid takes the shape of a paraboloid; in a rectangular domain, the radial variation of the fluid depth is defined as

$$H(r) = H_0 + \frac{\Omega^2}{2g}\left(r^2 - \frac{L_x^2 + L_y^2}{12}\right) \tag{1}$$

where H_0 is the depth of the fluid at rest; Ω is the angular velocity of the tank; g is the acceleration due to gravity; and L_x and L_y are the tank dimensions. This creates a barotropic fluid distribution. In order to quantify

the "latitudinal" variation of the Coriolis term, the β-effect, we calculate the β term as follows:

$$\beta = \frac{2sr_m f_0}{H(r_m)} \tag{2}$$

where $s = \Omega^2/2g$; $f_0 = 2\Omega$; and $H(r_m)$ is the fluid depth at $r_m = R/2$ (with R as the maximum radial distance).

Using NaCl as an electrolyte in water creates an electrolytic solution with an even concentration of Na^+ and Cl^- ions. An array of magnets placed under the tank create a magnetic field up through the tank, so that a current applied to the fluid results in movement of Na^+ ions moving toward the cathode and Cl^- ions moving toward the anode, thus inducing a Lorenz force on the ions. The Lorenz force in absence of an external electric field is defined:

$$\vec{F_L} = \rho\vec{v} \times \vec{B} = \vec{J} \times \vec{B} \tag{3}$$

where q is the charge of the particle being acted on; $\rho = qA^{-1}$ is the charge density; $\vec{v}$ is the velocity of the ions; $\vec{J} = \rho\vec{v}$ is the current density, and $\vec{B}$ is the magnetic flux density.

A feature tracking software produces Lagrangian velocities and interpolates them into an Eulerian velocity field. The magnitude of this velocity field present inside the tank can be defined at a given time t by the ensemble average:

$$\overline{U}(t) = \frac{1}{N}\sum_{i,j=1}^{N}[u_{i,j}(t)^2 + v_{i,j}(t)^2]^{1/2} \tag{4}$$

where N is the number of samples in the velocity field. The ensemble average of the velocity field can be used to calculate the kinetic energy. However, we can neglect mass in this instance for an outcome of kinetic energy per unit mass:

$$K = \frac{1}{2}\overline{U}(t)^2 \tag{5}$$

which will be referred to as the kinetic energy (KE) for conciseness. By applying the Reynolds decomposition to the kinetic energy

$$K(t) = \overline{K} + K' \tag{6}$$

we can evaluate kinetic energy fluctuations associated to the ensemble. The autocorrelation function of the velocity field at a point can be calculated as:

$$R_{i,j}(\tau) = \overline{U_{i,j}(t)U_{i,j}(t+\tau)}$$

where τ is the time lag between velocity samples at the point (i, j), then we can take the ensemble average of the autocorrelation function as follows:

$$\overline{R}(\tau) = \frac{1}{N}\sum_{i,j=1}^{N}\overline{U_{i,j}(t)U_{i,j}(t+\tau)}$$

Important variables in the topic of geophysical flows are that of vorticity. Of particular interest is the potential vorticity, q, defined as:

$$q = \frac{\zeta + f}{H(r)} \tag{7}$$

where $\zeta = \nabla \times \vec{v}$ is the relative vorticity, and $H(r)$ is the fluid depth defined earlier. The absolute vorticity $\zeta_a = \zeta + f$ in a 2D non-divergent field is a conserved quantity [17] and for a quasi-2D flow on a beta plane without external forces [3], it has been shown that:

$$\frac{D}{Dt}(q) = 0 \tag{8}$$

Which can inadvertantly be used as a good indicator of the accuracy of the feature tracking software. In the presence of external forcing, then, it seems reasonable to assume the following relation:

$$\frac{D}{Dt}|\zeta| \propto \frac{D}{Dt}K \tag{9}$$

3 Experimental Setup and Procedure

This experiment was performed using a rectangular tank of 68 x 68 x 15 cm^3. The tank was filled to a height H_0 of (height of fluid) with a saline solution of concentration $\sim$80$-$100 g/l. A circular array of permanent magnets were mounted underneath the tank so that a voltage applied to metal electrodes inside the tank resulted in a force on the electrolytic particles of the solution in accordance with Equation 3. Styrene particles with a mean diameter of $\sim 50\mu$m were added to the fluid surface to allow velocity field measurement. A camera mounted above the tank on the spinning apparatus imaged the tank at 20 frames/s with a resolution of 1023 x 1240 pixels, which were stored in a computer spinning with the tank. The tank was held on a large apparatus capable of spinning at a precise angular velocity, causing the fluid in the tank to take on a parabolic shape as described in Equation 1, and as seen in Figure 1.

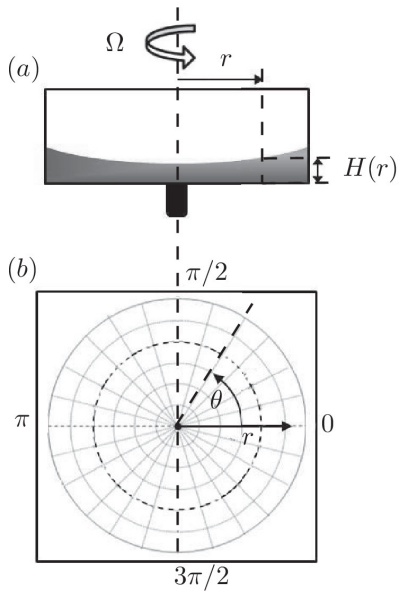

Figure 1: Diagram of tank rotation with resulting parabolic surface formation. Adapted from Di Nitto et al. [4]

This experiment was divided into two parts, the first being the flow evolution and the second being the flow decay. The tank was first accelerated to an angular velocity of $\Omega = 2\ s^{-1}$. When the fluid reached solid-body rotation, a voltage was applied across the electrodes inside the fluid, marking the beginning of the flow evolution at $t = 0$ seconds. The camera captured frames starting from when the voltage was applied and frames were stored in the attached computer. The flow decay was then recorded by turning off the applied current in a matured forced flow, the switching off of the current marks the $t = 0$ point of the flow decay process. The frames were post processed using a feature tracking software that reconstructs particle trajectories from displacements between subsequent frames and produces instantaneous Lagrangian velocities [18]. The time history of the Eulerian velocity field was then obtained by interpolating the sparse data over a regular grid. The time history of the velocity fields were stored as .mtr files for analysis. The final velocity grid was 128 x 128 for a length of approximately 250 s or approximately 5000 frames.

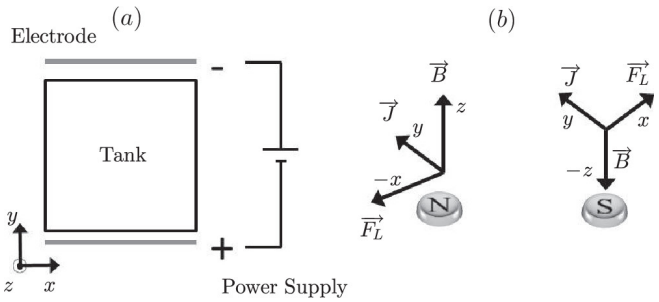

Figure 2: Sketch of the forcing system and resulting Lorenz force on particles above respective directed magnets. Adapted from Di Nitto et al. [4]

4 Results and Discussion

The presence of forcing in addition to the background rotation resulted in the emergence of a zonal jet countering the direction of rotation with both cyclonic and anticyclonic eddies, as well as the formation of a strong polar vortex. The evolution of the flow and its quantitative characteristics have been analyzed from Eulerian velocity fields deduced from the Images of the tank via the Feature Tracking software.

4.1 Average Velocities and Energy

The time history (Fig. 3) indicates the effect electromagnetic forcing has on a fluid in rigid-body rotation. The evolution experiment shows an increases the average velocity from a baseline of 0.075 cm s^{-1} to a mature flow at 0.275cm s^{-1}, the initial kinetic energy follows from 0.005 cm^2 s^{-2} to ∼0.004 cm^2 s^{-2} and peak kinetic energy fluctuation at the onset of forcing of approximately 0.017 cm^2 s^{-4}, with flow maturity reached at approximately 50 seconds. Peak values in the decay experiment varied from that of the evolution; possible reasons for this are discussed later. Average velocity during the decay experiment fell from approximately 0.19 cm s^{-1} to the baseline of ∼0.075 cm s^{-1} at 40 seconds of decay. KE and KE fluctuation saw similar baselines as the evolution experiment but with peak values at approximately half of those for the evolution.

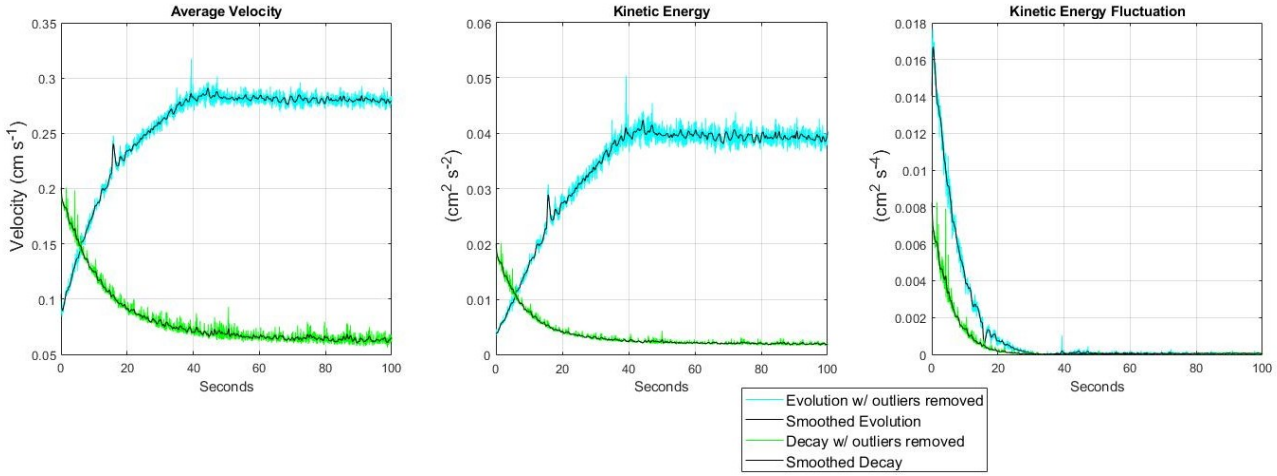

Figure 3: Time history of (a) the average velocity, (b) the average kinetic energy and (c) the kinetic energy fluctuations during the forced flow evolution and decay.

The Average velocity (Fig. 3a), kinetic energy (Fig. 3b), KE fluctuation (Fig. 3c), radial velocity (Fig. 4a) and azimuthal velocity (Fig. 4b) during the evolution experiment all exhibit an anomaly at approximately 15 seconds of evolution. Based on the data obtained, it is unclear at this time if this anomaly is due to a physical event during the evolution or due to a feature tracking inaccuracy. The flow decay consisted of halting the applied electrical forcing on a matured forced flow. The average velocity (Fig. 3) and kinetic energy (Fig. 3) decay to baseline between 80-100 seconds after forcing termination; however, KE fluctuation (Fig. 3) reaches baseline approximately 30 seconds after forcing termination. The time history of the average radial and azimuthal velocities (Fig. 4) for the decay experiment indicate more distinct differences in both relaxation time and behavior. The average radial velocity appears to decay more rapidly than the azimuthal velocity, approaching the baseline at approximately 30 seconds after force halting, with continuous radial velocity oscillations long past baseline is reached. In contrast, the average azimuthal velocity decays more slowly, approaching the baseline from 80-100 seconds after forcing termination.

While the zonation of the flow was of particular interest in this experiment, the time history of the average azimuthal velocity in Figure 4b holds little peculiarity to the zonal evolution in comparison to the time history of the average radial velocity seen in Figure 4a. The average radial velocity increases insignificantly until approximately 30 seconds during barotropic breakup (emergence of Rossby waves), where the average radial velocity increases to a peak around 40-50 seconds. Curiously, the average radial velocity then relaxes until 70-80 seconds where the radial velocity does not significantly change further.

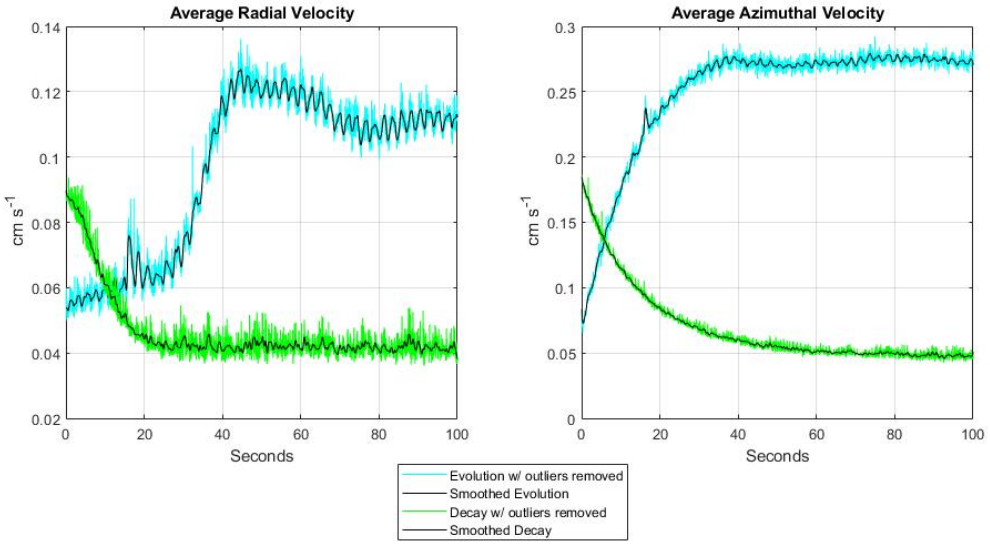

Figure 4: Time history of the average radial and azimuthal (zonal) velocity.

4.2 Zonal and Radial Velocity Fields

Snap shots of the azimuthal velocity field in Figure 5 show the emergence of the zonal jet which holds a slight presence even at the initialization of forcing, with parts of the jet reaching maximum zonal velocity within 5 seconds. Barotropic waves (Rossby waves) emerge in the zonal velocity field between approximately 27-30 seconds into forcing evolution. Later on in the evolution, a relatively strong azimuthal velocity emerges in the polar region, countering the flow of the zonal jet.

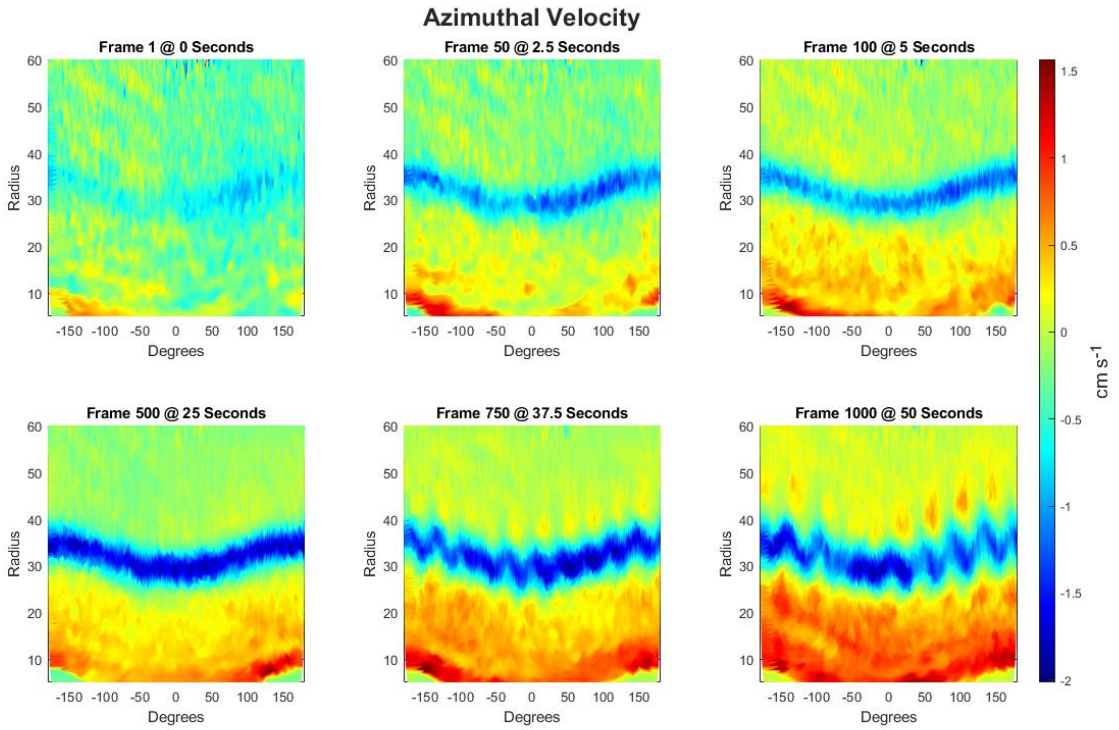

Figure 5: Snap shots of the zonal (azimuthal) velocity field showing the emergence and evolution of the zonal jet at: a) 0 seconds; b) 2.5 seconds; c) 5 seconds; d) 25 seconds; e) 37.5 seconds and f) 50 seconds.

A distinct difference between the zonal velocity field during the evolution (Fig. 5) and during the decay (Fig.

6) is in the velocity radially above and below the jet, which showed a strong zonal velocity countering the jet on both the polar and equatorial side after forcing was halted. At 15 seconds of decay, the fields on the either side of the jet were near baseline; however, the jet still showed strong presence. At 25 seconds of decay the zonal jet had diminished significantly and was no longer continuous. Despite this the azimuthal field retained differences between the jet region and the regions on either side. At 35 seconds of decay, the zonal velocity field had relaxed significantly, with only slightly elevated values around the latitude of the jet and random places toward the polar vortex.

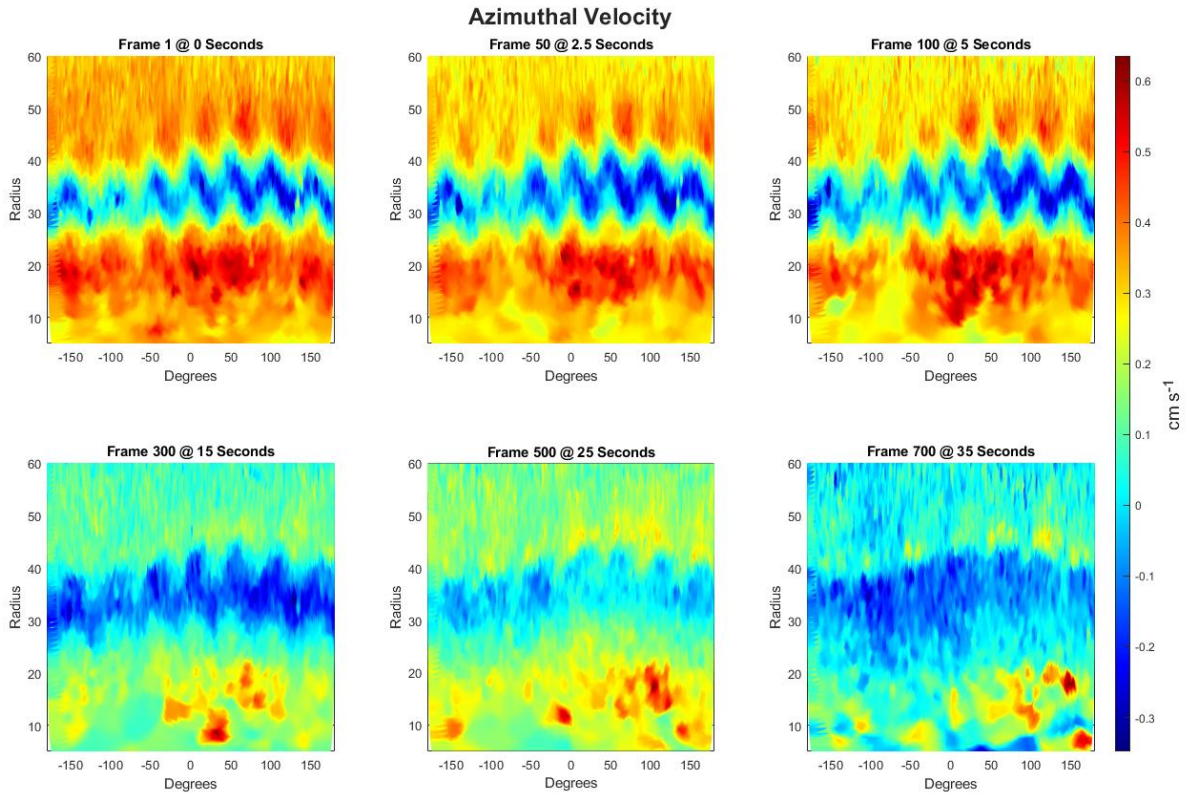

Figure 6: Decay of the jet in the zonal (azimuthal) velocity field at: a) 0 seconds; b) 2.5 seconds; c) 5 seconds; d) 15 seconds; e) 25 seconds and f) 35 seconds.

Snap shots of the radial velocity field evolution are shown in Figure 7. In contrast with quick emergence of the zonal jet, only small scale radial structures are present in the flow until barotropic waves begin to form between approximately 25-37 s. Alternating directional radial flow striations appear along the latitude of the zonal jet, with velocities in the respective flows reaching ± 1 cm s^{-1}. The radial flow structures grow from a (radial) length of approximately 3-5 cm at 25 seconds to 10-30cm after 50 s of evolution.

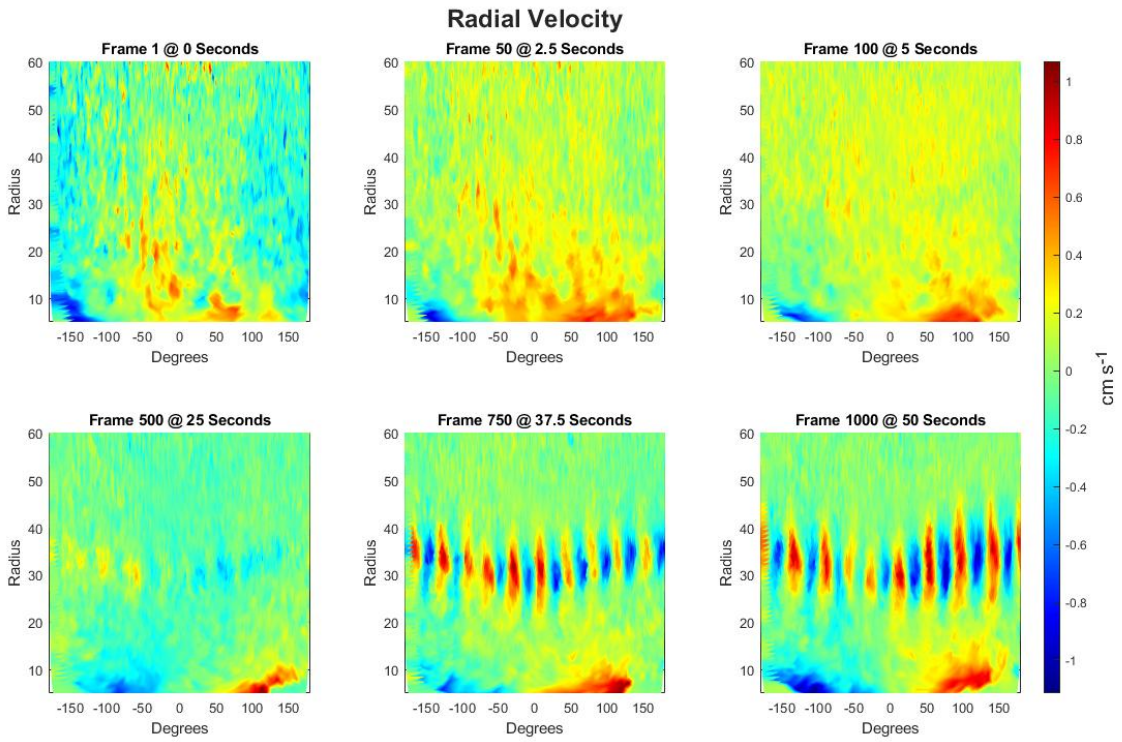

Figure 7: Snap shots of the radial velocity field evolution at: a) 0 seconds; b) 50 seconds; c) 100 seconds; d) 500 seconds; e) 750 seconds and f) 1000 seconds, showing the emergence of radial flow structures coherent with the zonal jet breaking up into Rossby waves.

The radial velocity field during the decay experiment shows the radial structures decaying in intensity at first but not in size. After 5 seconds of decay, the flow structures have reduced in intensity, but have slightly increased in length. After 15 s of decay the radial flow structures are still present, but much less coherent. After 25 s of decay, the radial flow structures along the zonal jet latitude are no longer dominant, but there remains striations of radial flow.

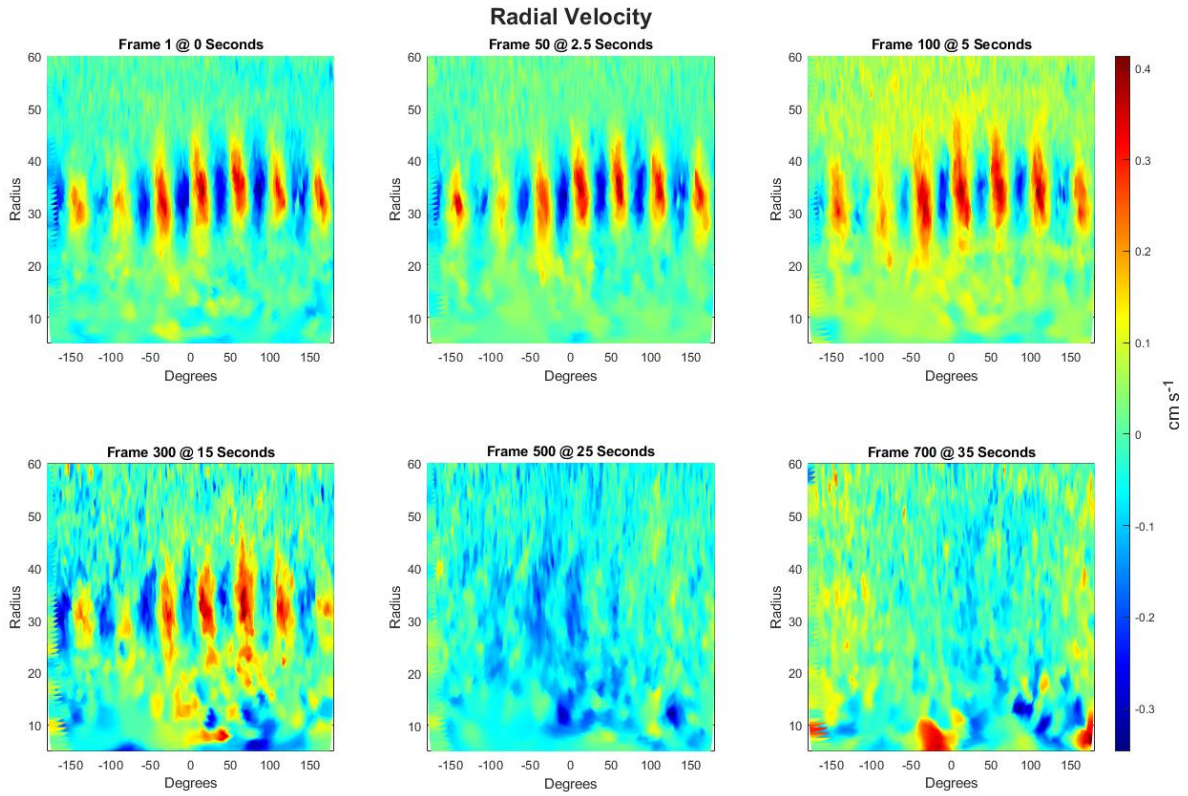

Figure 8: Decay of the radial velocity field a) 0 seconds; b) 2.5 seconds; c) 5 seconds; d) 15 seconds; e) 25 seconds and f) 35 seconds.

4.3 Vorticity and Potential Vorticity

Snap shots of the relative vorticity field and potential vorticity field during the evolution are shown in Figure 9 and Figure 10, respectively. The initiation of the forcing leads to an evolution of the flow starting with the emergence of the zonal jet. At 25 seconds into the evolution (Figures 9a and 10d), the zonal jet has reached a period of relative stability, which is distinct period visible in the time history of the average velocity (Fig. 3a), the kinetic energy (Fig. 3b) and the kinetic energy fluctuations (Fig. 3c) between roughly 22-30 seconds of the evolution. Barotropic instability across the zonal jet causes it to break up into barotropic waves (Rossby waves) as seen in Figures 9c-f and 10e-f. The presence of Rossby waves in the zonal jet become the stable state when the forced flow reaches maturity.

The overlay of relative vorticity with the velocity field in the first quadrant is shown in Figure 9. Vorticity values during the evolution of $\sim$-0.2 s^{-1} around the inside of the initial emergence of the jet and $\sim$0.2 s^{-1} on the outside. Eddies first appear at the onset of barotropic wave formation between 25 and 30 seconds of evolution. Positive vorticity values ($\sim$0.2 s^{-1}–0.6 s^{-1}) are associated to anticyclonic eddies on the outer side of the jet, and negative vorticity values ($\sim$-0.2 s^{-1} - -0.4 s^{-1}) associated to cyclonic eddies on the inside of the jet.

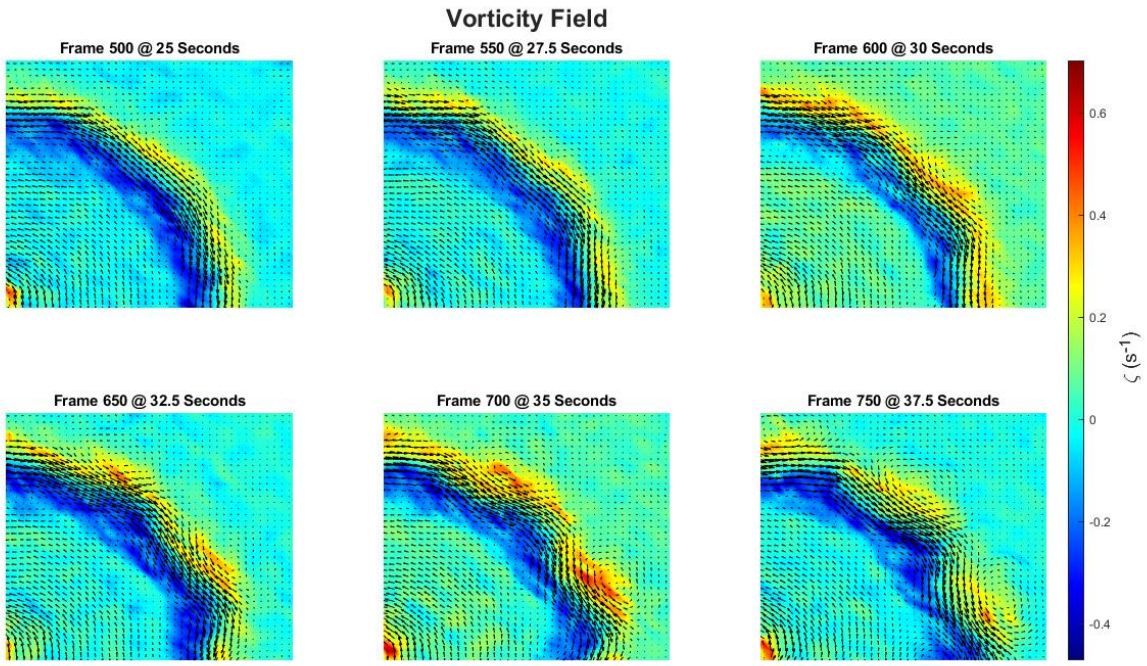

Figure 9: Evolution of the relative vorticity (color) and velocity field (arrows) at (a) 0 seconds, (b) 2.5 seconds, (c) 5 seconds, (d) 25 seconds, (e) 37.5 seconds and (f) 50 seconds.

Figure 10 shows snap shots of the potential vorticity field in the first quadrant during the evolution. At the initiation of forcing there is a distinct background PV gradient that remains coherent during the first 5 seconds of evolution. At 25 s of evolution, the PV field shows slight modification to this background gradient, with fluctuating values radially across the jet. At 37.5 s, mixing in the PV is clear and becomes more prevalent as forcing evolution continues. At 50 s, PV mixing around the zonal jet latitude show fluctuation of PV values between 0.35 $cm^{-1}s^{-1}$ and 0.4 $cm^{-1}s^{-1}$, with higher PV values being lifted toward the anticyclonic eddies and lower PV values bridging the jet toward the cyclonic eddies.

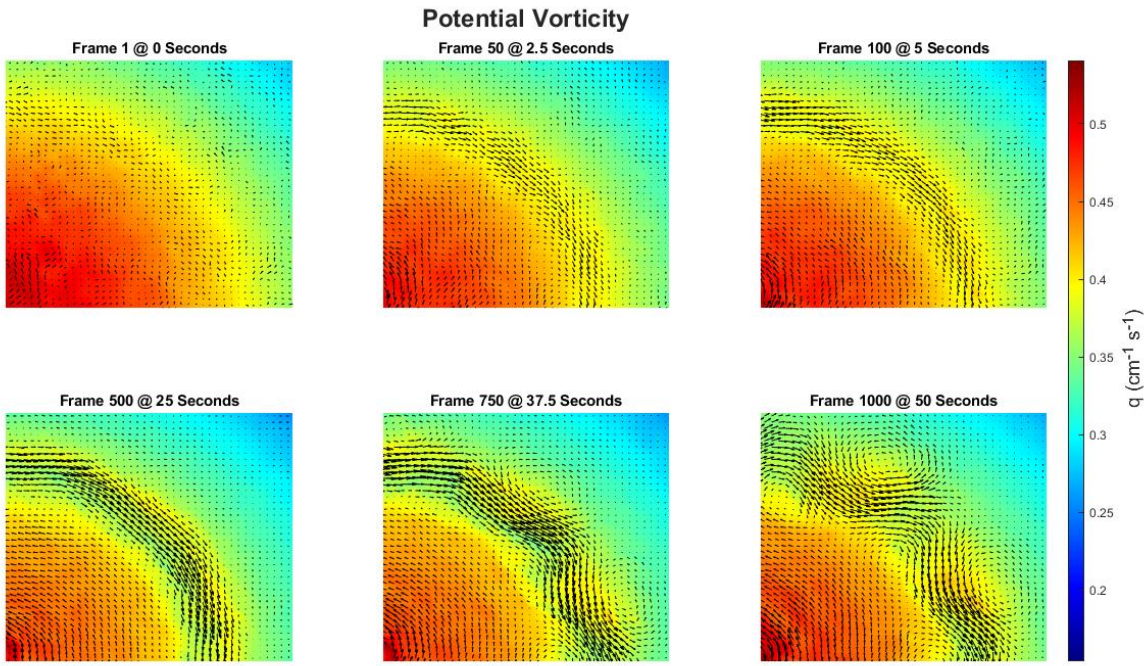

Figure 10: Evolution of the potential vorticity (color) and velocity field (arrows) at (a) 0 seconds, (b) 2.5 seconds, (c) 5 seconds, (d) 25 seconds, (e) 37.5 seconds and (f) 50 seconds.

The length of the mature waves were approximated from Figures 5 and 11 to 45 degrees in azimuthal (a result comparable to baroclinic waves present in the Earth's polar front jet stream) and ∼10 cm in (radial) height.

The mature flow structures generated are better visualized by averaging out the higher vorticity values in the polar vortex as seen in Figure 11, better revealing the turbulence and PV mixing around the zonal jet.

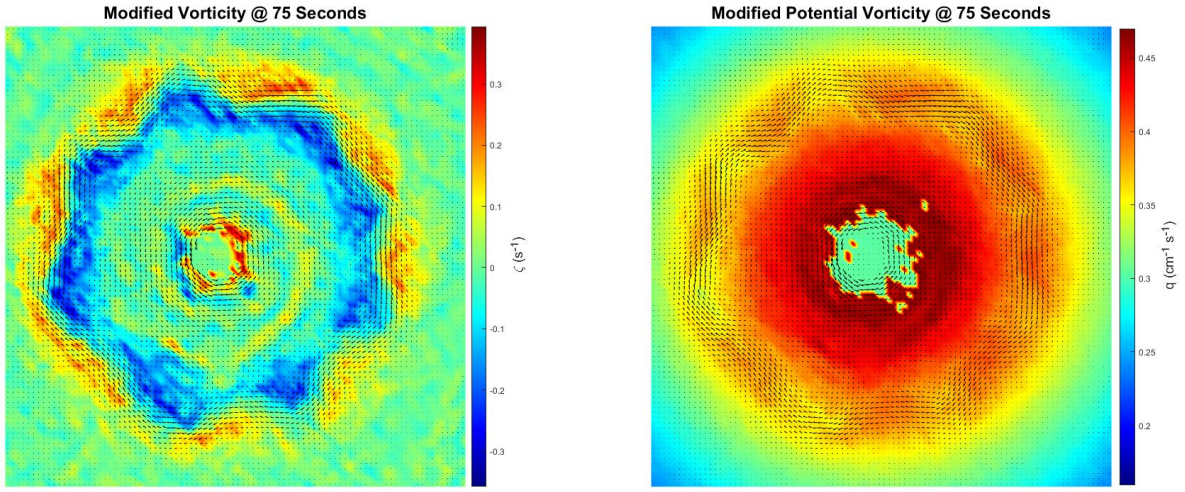

(a) (b)

Figure 11: Modified vorticity and potential vorticity fields at 75 seconds (Frame 1500) of evolution. Values above a certain threshold (in the polar vortex) have been reduced to the mean, allowing further visual exaggeration of vorticity around the jet.

The vorticity field decay (Fig. 13) reveals minimal decreases in vorticity around the eddies at 5 s after forcing termination, with more significant changes visible after 10 seconds of decay. As the zonal flow diminishes, larger areas of positive and negative vorticity associated to larger eddies break up into smaller eddies (and smaller areas of positive and negative vorticity); this is the (forward) energy cascade. After 25 s of decay the flow has diminished significantly with only slightly elevated ζ values associated to the outer side of the jets remnants.

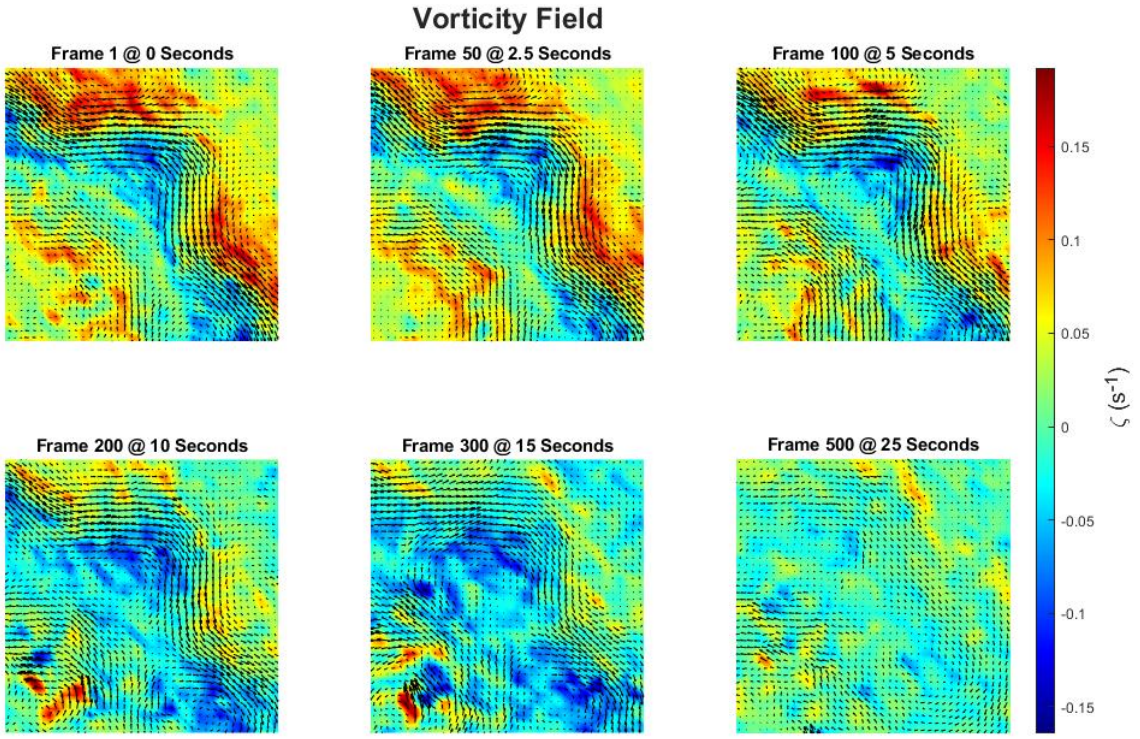

Figure 12: Decay of the vorticity (color) and velocity field (arrows).

Figure 13 shows snap shots of the PV field during the decay; here the modified field was used to enhance the PV mixing around the zonal jet, which is visible only in the first three frames from 0 s to 5 s. At 25 s of decay PV mixing has diminished with the background PV gradient reinstituted.

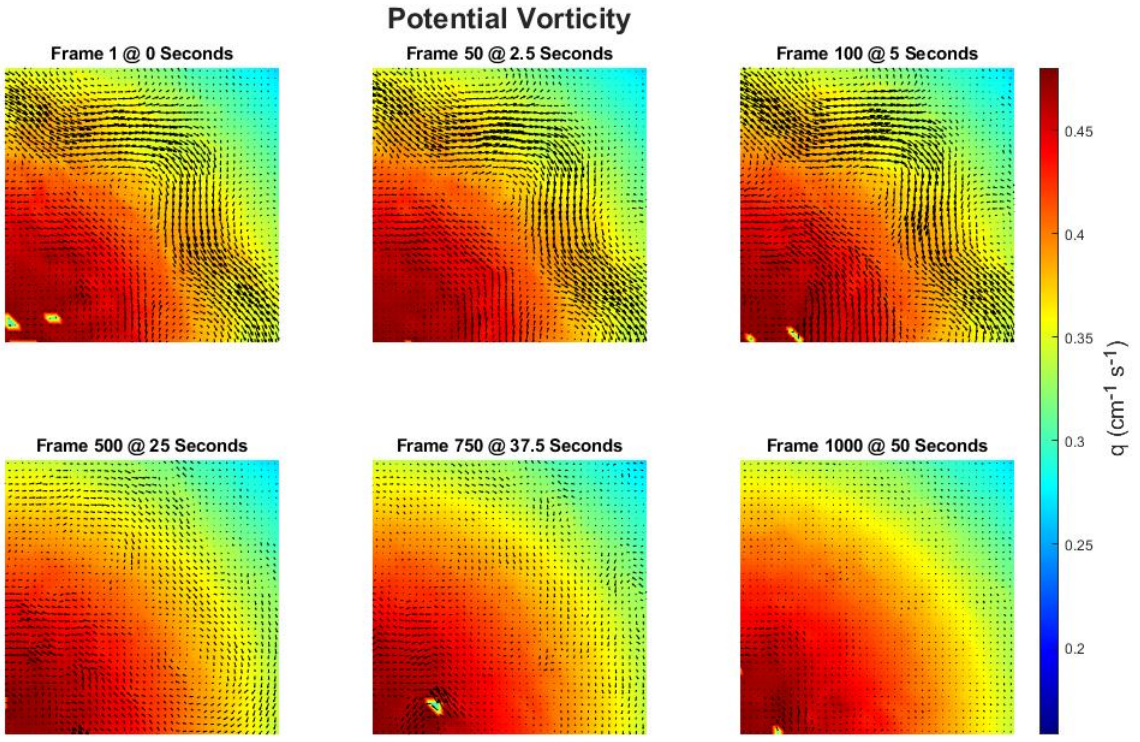

Figure 13: Decay of the potential vorticity (color) and velocity field (arrows).

5 Conclusions

Overall, electromagnetic forcing proves to be a good method for simulating zonal flows. This simulation was able to reproduce a single zonal jet that broke up into Rossby waves with azimuthal wavelength mimicking that of the Polar-front jet stream in Earth's atmosphere. Anticyclonic eddies on the outside of the jet were associated to positive vorticity values and cyclonic eddies on the inside associated with negative vorticity values. Spikes in the average velocities and KE time history between ∼15-20 seconds appear to be associated with higher velocity field around the polar vortex region. A zonal jet emerged soon after forcing on the approximately uniform background potential vorticity gradient. Random small scale vortices contributed to the formation of larger scale vortices with PV mixing and Rossby wave formation through inverse energy cascade.

The evolution and decay experiments differ in peak values, in terms of starting values for the decay experiment and ending values of the evolution experiment. It is unclear if this is due to the decay experiment being started prematurely, if the decay recording was delayed, or if the discrepancy is due to feature tracking software inaccuracies: the similarity in baseline values of the average velocity would give weight to the two former possibilities, but comparing the average radial velocity baselines may indicate the latter.

References

[1] A. Sanchez-Lavega. *An Introduction to Planetary Atmospheres*. Taylor & Francis, 2011.

[2] Ann Ewing. Jet stream steers weather. *The Science News-Letter*, 66(23):362–364, 1954.

[3] C-G. Rossby. Planetary flow patterns in the atmosphere. *Quarterly journal of Royal meteorological society*, 66:68–87, 1940.

[4] G. Di Nitto, S. Espa, and A. Cenedese. Simulating zonation in geophysical flows by laboratory experiments. *Physics of Fluids*, 25(8):086602, 2013.

[5] Boris Galperin, Jesse Hoemann, Stefania Espa, Gabriella Di Nitto, and Guglielmo Lacorata. Anisotropic macroturbulence and diffusion associated with a westward zonal jet: From laboratory to planetary atmospheres and oceans. *Phys. Rev. E*, 94:063102, Dec 2016.

[6] Mark P. Baldwin, Peter B. Rhines, Huei-Ping Huang, and Michael E. McIntyre. The jet-stream conundrum. *Science*, 315(5811):467–468, 2007.

[7] Boris Galperin, Hideyuki Nakano, Huei-Ping Huang, and Semion Sukoriansky. The ubiquitous zonal jets in the atmospheres of giant planets and earth's oceans. *Geophysical Research Letters*, 31(13), 2004.

[8] Balu Nadiga. On zonal jets in oceans, 2007.

[9] Boris Galperin, Semion Sukoriansky, and Nadejda Dikovskaya. Geophysical flows with anisotropic turbulence and dispersive waves: flows with a [beta]-effect. *Ocean Dynamics*, 60(2):427–441, 04 2010. Copyright - Copyright Springer Science & Business Media Apr 2010; Document feature - Diagrams; Equations; Graphs; ; Last updated - 2014-08-31.

[10] Isaac M. Held. The macroturbulence of the troposphere. *Tellus A: Dynamic Meteorology and Oceanography*, 51(1):59–70, 1999.

[11] D. G. Dritschel and M. E. McIntyre. Multiple jets as pv staircases: The phillips effect and the resilience of eddy-transport barriers. *Journal of the Atmospheric Sciences*, 65(3):855 – 874, 2008.

[12] Isabella Bordi, Klaus Fraedrich, Frank Lunkeit, and Alfonso Sutera. Tropospheric double jets, meridional cells, and eddies: A case study and idealized simulations. *Monthly Weather Review*, 135(9):3118–3133, 09 2007. Copyright - Copyright American Meteorological Society Sep 2007; Document feature - Graphs; Equations; Tables; ; Last updated - 2017-10-31; CODEN - MWREAB.

[13] Yohai Kaspi and Glenn R. Flierl. Formation of jets by baroclinic instability on gas planet atmospheres. *Journal of the Atmospheric Sciences*, 64(9):3177 – 3194, 2007.

[14] Paul A. O'Gorman and Tapio Schneider. Recovery of atmospheric flow statistics in a general circulation model without nonlinear eddy-eddy interactions. *Geophysical Research Letters*, 34(22), 2007.

[15] A. G. Slavin and Y. D. Afanasyev. Multiple zonal jets on the polar beta plane. *Physics of Fluids*, 24(1):016603, 2012.

[16] Semion Sukoriansky, Nadejda Dikovskaya, and Boris Galperin. On the arrest of inverse energy cascade and the rhines scale. *Journal of the Atmospheric Sciences*, 64(9):3312 – 3327, 2007.

[17] C-G. Rossby. Relation between variations in the intensity of the zonal circulation of the atmosphere and the displacements of the semi-permanent centers of action. *Journal of Marine Research*, 2:38–55, 1939.

[18] Monica Moroni and Antonio Cenedese. Comparison among feature tracking and more consolidated velocimetry image analysis techniques in a fully developed turbulent channel flow. *Measurement Science and Technology*, 16(11):2307–2322, oct 2005.